

Implications for unified schemes from submillimetre and far-infrared follow-up of radio-selected samples

Jennifer A. Grimes¹, Steve Rawlings^{1*} and Chris J. Willott^{1,2}

¹*University of Oxford, Astrophysics, Keble Road, Oxford, OX1 3RH, UK*

²*Herzberg Institute of Astrophysics, National Research Council, 5071 West Saanich Road, Victoria, BC, V9E 2E7, Canada*

21 June 2018

ABSTRACT

We extend our previous analysis which used generalized luminosity functions (GLFs) to predict the number of quasars and galaxies in low-radio-frequency-selected samples as a function of redshift, radio luminosity, narrow-emission-line luminosity and type of unified scheme (Grimes, Rawlings & Willott 2004). Our extended analysis incorporates the observed submillimetre (850 μm) flux densities of radio sources, employs a new method which allows us to deal with non detections, and focuses on the high-luminosity population. First, we conclude that the submillimetre luminosity L_{850} of low-frequency-selected radio sources is correlated with the bolometric luminosity L_{Bol} of their quasar nuclei via an approximate scaling relation $L_{850} \propto L_{\text{Bol}}^{0.7 \pm 0.2}$. Second, we conclude that there is quantitative evidence for a receding-torus-like physical process for the high-luminosity population within a two-population unified scheme for radio sources; this evidence comes from the fact that radio quasars are brighter in both narrow emission lines and submillimetre luminosity than radio galaxies matched in radio luminosity and redshift. Third, we note that the combination of a receding-torus-like scheme and the assumption that the observed submillimetre emission is dominated by quasar-heated dust yields a scaling relation $L_{850} \propto L_{\text{Bol}}^{0.5}$ which is within the errors of that determined here for radio-selected quasars, and consistent with that inferred for radio-quiet quasars by Willott, Rawlings & Grimes (2003).

Key words: galaxies: active – quasars: general – galaxies: evolution

1 INTRODUCTION

Unified schemes for radio galaxies and radio quasars propose that both types of objects are physically similar but viewed at different angles between the radio axis and the line of sight. A comprehensive introduction to the subtleties involved in such schemes can be found in Grimes, Rawlings & Willott (2004, hereafter GRW) in which we presented a method of using generalized luminosity functions (GLFs) to predict the number of radio galaxies and radio-loud quasars as a function of redshift z , radio luminosity, narrow-emission-line luminosity and type of unified scheme. The GRW analysis introduced two new parameters: α encoding the well known, and strong, correlation between radio and narrow-line luminosity; and β encoding the scatter about this relation. GRW concluded that the simplest unified schemes, in which the probability of a given object being viewed as a quasar is independent of α , are

strongly ruled out by the data available on radio-selected samples. However, their analysis was unable to discriminate between the two most popular modifications to the simplest schemes, namely: (i) models in which the probability of a given object being viewed as quasar is dependent on α and β , as in the ‘receding torus’ scheme (Lawrence 1991; Simpson 1998); and (ii) models in which there are two populations of radio sources, only one of which necessarily comprises of an admixture of unobscured and obscured quasar nuclei (Willott et al. 2000). Both modified schemes were able to explain both the systematic increase in the fraction of quasars with α and the systematically higher narrow-emission-line luminosities for radio quasars over radio galaxies, matched in radio luminosity and redshift.

Differences in luminosities between samples of radio quasars and radio galaxies, matched in radio luminosity and redshift, have also been found at submillimetre and infrared wavelengths (e.g. Willott et al. 2002a). These wavebands would seem to be ideal for testing unified schemes. The putative opaque dust torus is a vital ingredient of all

*Contact email: sr@astro.ox.ac.uk

unified schemes as it is needed to hide the active nucleus by absorbing the soft X-ray, UV, optical and near-infrared radiation. Much of this absorbed energy will be re-radiated by dust grains at infrared wavelengths, and for high-redshift objects this may be observed in the submillimetre waveband. This dust is expected to be optically thin (at least at longer wavelengths) and its thermal emission is radiated isotropically (Efsthathiou & Rowan-Robinson 1994).

Willott et al. (2002a) found that radio-loud quasars were a factor of approximately 2 – 5 times brighter than radio galaxies from SCUBA data at 850 μm , where the large uncertainty arises because of the difficulties involved with correcting the submillimetre flux densities for synchrotron contamination. However, earlier studies of far-infrared differences between quasars and radio galaxies led to conflicting results. Broad-lined objects were found to be more luminous than narrow-lined objects in the far-infrared from four pairs of objects in the redshift range $0.25 < z < 0.57$ (van Bemmell, Barthel & de Graauw 2000), whereas Meisenheimer et al. (2001) found no difference in the mid- and far-infrared flux densities of ten pairs of radio galaxies and radio quasars with $z \leq 2$. Such results have led to discussions of the viability of unified schemes for radio-selected quasars and galaxies.

In this paper, submillimetre data on radio-selected samples will be incorporated into the GLF approach of GRW. The availability of submillimetre data for complete samples of radio sources is much more limited than is the case for narrow emission-line data, and non detections are far more common. However, the available submillimetre data has been collected in a way that yields quantifiable biases. We have four main aims. First, to discriminate robustly between the competing unified models that were considered in GRW. Second, to quantify the correlation between α and submillimetre (850 μm) luminosity L_{850} , leading to an estimate of the correlation between (the unobscured) optical quasar luminosity M_B (or, equivalently, bolometric quasar luminosity L_{Bol}) of radio sources and L_{850} . Third, to obtain increased predictive power for the GLFs due to the addition of submillimetre data. Fourth, to understand the discrepancies between previous studies of differences between radio galaxies and quasars in the far-infrared and submillimetre.

This paper is organized as follows. In Sec. 2, the data to be used are described. In Sec. 3, the correlations between submillimetre luminosity and the principal components found in GRW are investigated. In Sec. 4, new GLFs based on this correlation are described and the results and analysis are presented. We make comparisons between the predictions of our GLFs and previous studies in Sec. 5. In Sec. 6 we derive a scaling relation between far-infrared luminosity and the bolometric luminosity of the quasar nuclei of radio sources. We assume throughout that $H_0 = 70 \text{ km s}^{-1} \text{ Mpc}^{-1}$, $\Omega_M = 0.3$ and $\Omega_\Lambda = 0.7$.

2 DATA

A sample of eighteen high-redshift ($1.3 < z < 3.5$) radio quasars with existing 850- μm SCUBA data has been defined. These are drawn from a suite of low-frequency-selected redshift surveys: the 3CRR sample (Laing, Riley & Longair 1983), the 3CR sample (Spinrad et al. 1985); the 6CE

sample (Rawlings, Eales & Lacy 2001); parts I and II of the 7CRS sample (Willott et al. 2002b); and the TOOT (TEXOX-1000) Survey (Hill & Rawlings 2003). The first four of these surveys have complete optical identifications and essentially complete spectroscopic redshifts (or, in the case of the 7CRS, reliable photometric redshifts for the few objects without secure spectroscopic values). The subsections of the TOOT survey used in this work have complete spectroscopy but significantly lower redshift completeness (Hill & Rawlings 2003): we are confident, however, that few, if any, quasars with $R \leq 23.5$ have been overlooked.

Willott et al. (2002a) presented SCUBA data for eleven quasars in the redshift range $1.37 < z < 2.0$: two quasars from the 6CE sample with $2.0 \leq S_{151} \leq 3.93 \text{ Jy}$ (6C 0955+3844 and 6C 1045+3513); seven quasars from the 3CRR sample, within the Right Ascension (RA) range $04^{\text{h}} < \text{RA} < 22^{\text{h}}$; and two quasars (3C 298 and 3C 280.1) from the 3CR catalogue, which were not included in the 3CRR for reasons of low declination and (slightly) low radio flux-density respectively. The sky area for the combined 3CRR/3CR subsample was estimated by taking $\frac{9}{10}$ of the sky area that the 3CR survey would have with the reduced RA range, since all of the 3CRR objects are included in the 3CR survey, but one 3CR object (3C 418) is in the correct redshift and RA range but could not be considered here because it has no SCUBA data.

Rawlings et al. (2004) presented submillimetre data for eight quasars with $2.5 \leq z \leq 3.5$: five radio quasars selected from the TOOT00 and TOOT08 sub-regions of the TOOT with $R \leq 23.5$ and $0.1 \leq S_{151} < 0.2 \text{ Jy}$, where S_{151} is the 151-MHz flux density; and three radio quasars from parts I and II of the 7CRS sample with $S_{151} > 0.5 \text{ Jy}$. We have halved the effective sky area of the 7CRS survey to account for the fact that only two out of four 7CRS quasars in the redshift range are used; this assumes that the excluded objects, synchrotron-dominated quasars (5C 6.288 and 5C 6.291; one of which was observed by Rawlings et al.), are unbiased with respect to their (isotropic) thermal dust luminosities.

The [OIII] luminosities of the TOOT objects were estimated from the Lyman- α line luminosities (which are dominated by emission from the narrow-line region) from Rawlings, Hill & Willott (2004) and converted to $L_{[\text{OIII}]}$ using the line ratios presented in McCarthy (1993). [There are uncertainties in this procedure because reddening can have a large impact on the $\text{Ly}\alpha / [\text{OIII}]$ ratio.]

For the two 7CRS objects, the [OIII] line luminosity was estimated by assuming a rest-frame equivalent width of 30 \AA for this line. For the 6CE and 3CR objects, the line luminosities are taken from Willott et al. (2002a), except 3C437 which had its [OIII] luminosity estimated using the [OIII]/[OII] relation from GRW, and 6C 0919+3806 which now correctly employs the CII/[OIII] ratio of McCarthy (1993).

Table 1 shows the basic data for the sample, including the α and β values derived following the prescription of GRW. Submillimetre luminosity is used as a measure of the radiation from dust, which may be heated by star-formation and/or the central quasar nucleus. However, since the 6CE and 3CR samples include high-flux-density radio sources, it is necessary to attempt to correct for contamination of the submillimetre radiation by the synchrotron radiation

| Name | Class | Redshift z | D / kpc | $\log_{10}[L_{151}/$ $\text{WHz}^{-1}\text{sr}^{-1}]$ | $\log_{10}[L_{\text{[OIII]}}/$ $\text{W}]$ | $S_{850}/$ mJy | $S_{450}/$ mJy | SC | α | β |
|--------------|-------|-----------------|-----------------------|--|---|------------------------------------|-------------------------------------|------|----------|---------|
| TOOT00_1214 | Q | 3.084 | $\simeq 38.0^\dagger$ | 26.77 | 36.25 | 2.04 ± 1.18 | 3.80 ± 11.10 | 0.00 | 0.030 | -0.027 |
| TOOT00_1261 | Q | 2.544 | $\simeq 24.0^\dagger$ | 26.77 | 36.28 | 1.98 ± 1.31 | -18.90 ± 22.80 | 0.00 | 0.031 | -0.029 |
| TOOT08_061 | Q | 3.277 | < 41.0 | 27.06 | 36.89 | 8.59 ± 1.10 | 14.90 ± 5.70 | 0.00 | 0.065 | -0.040 |
| TOOT08_079 | Q | 3.002 | < 42.0 | 26.91 | 36.98 | 0.05 ± 1.14 | -2.50 ± 9.10 | 0.00 | 0.063 | -0.049 |
| TOOT08_094 | Q | 3.256 | < 42.0 | 27.20 | 35.82 | 0.91 ± 1.05 | -5.10 ± 6.50 | 0.00 | 0.031 | 0.005 |
| 5C 6.95 | Q | 2.877 | 119.3 | 27.55 | 36.41 | 2.40 ± 1.23 | 0.30 ± 13.40 | 0.00 | 0.067 | -0.004 |
| 5C 7.70 | Q | 2.617 | 14.4 | 27.75 | 35.35 | 0.32 ± 1.20 | 5.90 ± 14.80 | 0.00 | 0.035 | 0.043 |
| 3C 181 | Q | 1.382 | 48.0 | 28.11 | 37.37 | 5.27 ± 1.06 | -0.80 ± 7.50 | 0.06 | 0.124 | -0.018 |
| 3C 191 | Q | 1.952 | 41.1 | 28.52 | 37.21 | 6.39 ± 1.06 | 28.90 ± 8.10 | 0.30 | 0.133 | 0.005 |
| 3C 205 | Q | 1.534 | 152.4 | 28.19 | 37.00 | 2.36 ± 1.10 | 11.60 ± 7.90 | 0.52 | 0.113 | -0.001 |
| 3C 268.4 | Q | 1.400 | 91.9 | 27.97 | 37.25 | 5.13 ± 1.18 | 9.90 ± 12.50 | 0.58 | 0.114 | -0.018 |
| 3C 270.1 | Q | 1.519 | 101.6 | 28.24 | 36.51 | 7.42 ± 1.17 | 15.40 ± 11.50 | 0.40 | 0.097 | 0.020 |
| 3C 280.1 | Q | 1.659 | 39.8 | 28.36 | 36.72 | 5.10 ± 1.74 | 0.40 ± 23.80 | 0.35 | 0.109 | 0.016 |
| 3C 298 | Q | 1.439 | 12.7 | 28.57 | 37.26 | 21.13 ± 2.06 | -8.00 ± 23.70 | 0.38 | 0.137 | 0.005 |
| 3C 318 | Q | 1.574 | 6.8 | 28.11 | 37.18 | 7.78 ± 1.00 | 21.60 ± 10.60 | 0.00 | 0.116 | -0.010 |
| 3C 432 | Q | 1.785 | 109.8 | 28.32 | 36.68 | 7.93 ± 1.70 | 2.91 ± 20.90 | 0.05 | 0.106 | 0.016 |
| 6C 0995+3844 | Q | 1.405 | 181.3 | 27.45 | 36.58 | -0.01 ± 1.11 | 8.90 ± 7.80 | 0.00 | 0.069 | -0.014 |
| 6C 1045+3513 | Q | 1.594 | 1.7 | 27.22 | 35.94 | 9.18 ± 1.10 | 21.30 ± 6.80 | 0.05 | 0.036 | 0.001 |

Table 1. Submillimetre observations and basic data for the sample of eighteen radio quasars from Rawlings et al. (2004) and Willott et al. (2002a). The values for the [OIII] line strength have been calculated by various methods (see Sec. 2). Submillimetre detections at the $\geq 2\sigma$ level are given in bold type. SC is the assumed fractional synchrotron contamination at 850 μm . D is the projected linear size of the radio source and a \dagger denotes that it has been measured between the core and an extended component on just one side of the core. The synchrotron contaminations, expressed as fractions of observed S_{850} , were taken from Rawlings et al. (2004). The parameters α and β have been derived using the method of GRW.

responsible for radio emission. The fractional corrections for synchrotron contamination, included in Table 1 for the 6CE and 3CR sub-samples, were taken from Rawlings et al. (2004) and Willott et al. (2002a). Throughout this paper, submillimetre flux densities are converted to L_{850} by, first, correcting for synchrotron contamination and then, second, by assuming a grey body emission spectrum with a dust temperature $T_d = 40$ K and emissivity index $\beta_d \approx 2$ (Priddey & McMahon 2001).

Fig. 1 shows the objects in the sample as a function of L_{151} and z , in comparison to the full 3CRR/6CE/7CRS dataset used in GRW. In this paper we are clearly focusing on smaller samples at higher redshifts, but we still span a wide range of L_{151} because of the inclusion of TOOT data.

3 THE $L_{850} - \alpha$ CORRELATION

GRW encoded the $L_{\text{[OIII]}} - L_{151}$ correlation for radio sources using the parameters α and β , derived from a principal components analysis. In this section the correlations between submillimetre (850- μm) luminosity L_{850} , L_{151} , $L_{\text{[OIII]}}$ and α are investigated. The aim is to find the best way of incorporating submillimetre data into the GLFs derived by GRW.

3.1 New PCA Analysis

A new principal components analysis (PCA) was carried out to determine the nature of the correlation between L_{151} , $L_{\text{[OIII]}}$ and L_{850} . This analysis used the data of Sec. 2. Although the overall fraction of submillimetre detections is low amongst the fainter radio samples, such objects have been detected in a statistical sense (Rawlings et al. 2004). Therefore, we replaced any synchrotron-corrected values of S_{850} below the 1σ detection limit by this limit for the purposes of

| | $\lambda_{\alpha'}$ | $\lambda_{\beta'}$ | $\lambda_{\gamma'}$ |
|--|------------------------|-----------------------|------------------------|
| Eigenvalue | 1.93 | 0.57 | 0.50 |
| Proportion | 0.64 | 0.19 | 0.17 |
| | $\mathbf{e}_{\alpha'}$ | $\mathbf{e}_{\beta'}$ | $\mathbf{e}_{\gamma'}$ |
| $\log_{10}(L_{151})_{\text{norm}}$ | 0.593 | -0.024 | 0.805 |
| $\log_{10}(L_{\text{[OIII]}})_{\text{norm}}$ | 0.571 | -0.693 | -0.441 |
| $\log_{10}(L_{850})_{\text{norm}}$ | 0.569 | 0.720 | -0.397 |

Table 2. Table of the eigenvalues $\lambda_{\alpha'}$, $\lambda_{\beta'}$ and $\lambda_{\gamma'}$, and eigenvectors $\mathbf{e}_{\alpha'}$, $\mathbf{e}_{\beta'}$ and $\mathbf{e}_{\gamma'}$ from the PCA analysis, such that $\mathbf{e}_{\alpha'} = 0.593 \log_{10}(L_{151})_{\text{norm}} + 0.571 \log_{10}(L_{\text{[OIII]}})_{\text{norm}} + 0.569 \log_{10}(L_{850})_{\text{norm}}$ etc. The components are normalized in the same manner as GRW and primes are used to distinguish these principal components from those found in their previous, two-variable, PCA analysis.

calculating L_{850} . The mean values of $\log_{10} L_{151}$, $\log_{10} L_{\text{[OIII]}}$ and $\log_{10} L_{850}$ are 27.73, 36.65 and 22.68 respectively, with associated standard deviations 0.60, 0.55 and 0.38. The results of the PCA are given in Table 2. The dominant correlation (accounting for $\simeq \frac{2}{3}$ of the scatter) is a positive correlation between L_{850} , $L_{\text{[OIII]}}$ and L_{151} . To test if this 1σ -upper-limit approach yielded serious problems, we repeated the analysis with ten-times lower values of $\log_{10} L_{850}$ for the non-detections, which yielded only small changes in the derived values. Note, however, that this would increase the dispersion in $\log_{10} L_{850}$, so that the interpretation of the normalized quantities would be different.

3.2 Survival analysis

The new PCA (Sec. 3.1) has yielded the basic result that L_{850} is positively correlated with L_{151} and $L_{\text{[OIII]}}$. As the α parameter from GRW encodes the L_{151} and $L_{\text{[OIII]}}$ correlation, it is expected that L_{850} will be correlated with α . In

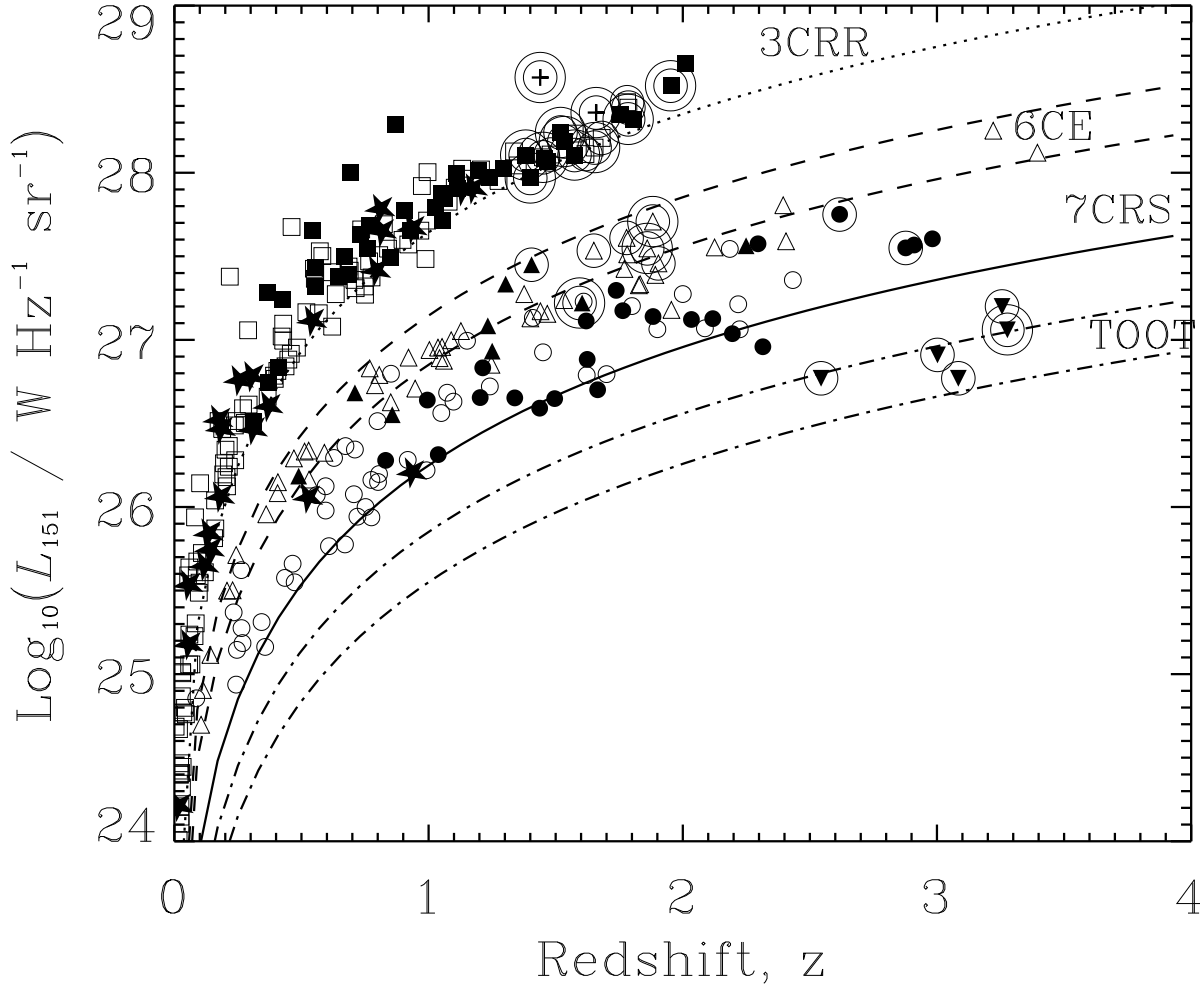


Figure 1. The 151 MHz luminosity L_{151} versus redshift z plane for the 3CRR, 6CE and 7CRS complete samples with the symbols identifying radio quasars and radio galaxies from different samples: 3CRR quasars (filled squares); 3CRR radio galaxies (open squares); 6CE quasars (filled triangles); 6CE radio galaxies (open triangles); 7CRS quasars (filled circles); and 7CRS radio galaxies (open circles). Weak quasars (see GRW) are identified by star symbols. Also shown are the five TOOT quasars (inverted triangles), and the two 3CR quasars (plus signs) described in Sec. 2. Circles surrounding symbols show objects observed by SCUBA, and additional larger circles show objects detected by SCUBA at the $> 2\sigma$ level. The dotted line shows the flux-density lower limit for the 3CRR sample, the dashed lines show the upper and lower limits for 6CE, the solid line shows the lower limit for 7CRS and the dot-dashed lines show the upper and lower limits for the TOOT sample (all assuming a radio spectral index of 0.8).

this section, a survival analysis is used to quantify the correlation between $\log_{10} L_{850}$ and the $\log_{10} L_{151}, \log_{10} L_{[\text{OIII}]}$ combination through α , now taking into account the 2σ upper limits which are important because nearly half of the objects are not detected at the 2σ level at $850\mu\text{m}$. A correlation and regression analysis was carried out using the ASURV software (Isobe, Feigelson & Nelson 1986).

Table 3 shows the correlation coefficients using three methods: Cox’s Proportional Hazard model, the generalized Kendall’s rank correlation test for censored data sets using the BHK test, both of which measure the degree of association of two variables, and the Buckley–James method which

is the usual least squares regression adapted for censored data. Fig. 2 shows the correlations of L_{850} with L_{151} and $L_{[\text{OIII}]}$, and also the correlation of L_{850} with α .

This battery of statistical tests suggests that there are real, positive correlations between the variables considered. However, the best-fit lines are strongly dependent on how the upper limits are treated. In the next section we will extend the GLFs from GRW to encode the $L_{850} - \alpha$ correlation and to treat upper limits in a way more appropriate to the problem under consideration.

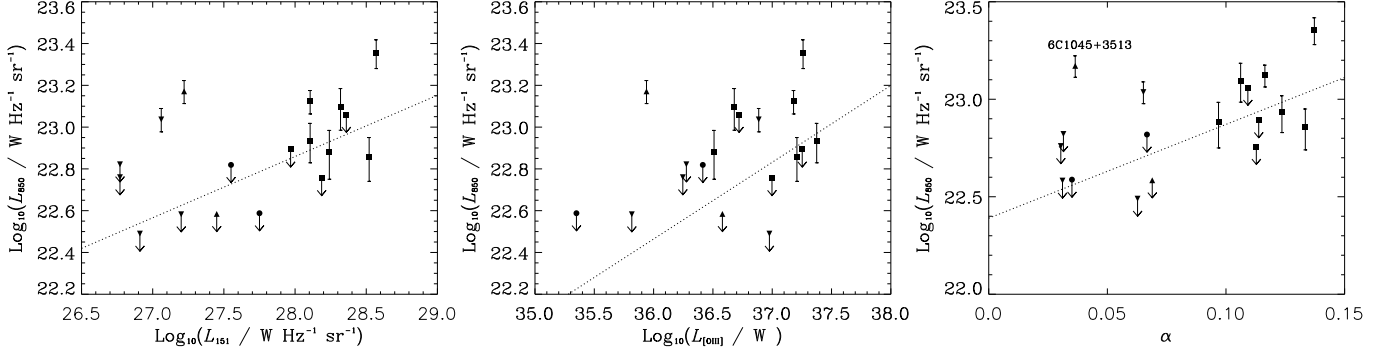


Figure 2. The correlations of $\log_{10} L_{850}$ with $\log_{10} L_{151}$, $\log_{10} L_{[\text{OIII}]}$ and α for the sample of eighteen quasars defined in Table 1. The 2σ upper limits are shown for the non-detections (symbols as in Fig. 1). The best-fitting (dotted) lines are shown from an analysis using the Buckley–James method.

| Correlation of $\log_{10} L_{850}$ with | Cox Prop Hazard | | BHK test | | | Buckley–James Method | | | |
|--|-----------------|-------|----------|-------|-------|----------------------|----------|------|------|
| | χ^2 | P_c | τ | Z | P_k | Intercept | Gradient | SD | SDR |
| $\log_{10} L_{151}$ | 3.632 | 0.057 | 0.523 | 1.744 | 0.081 | 14.65 | 0.29 | 0.17 | 0.26 |
| $\log_{10} L_{[\text{OIII}]}$ | 2.459 | 0.117 | 0.444 | 1.482 | 0.139 | 9.23 | 0.21 | 0.21 | 0.27 |
| α | 4.352 | 0.037 | 0.575 | 1.917 | 0.055 | 22.39 | 4.81 | 2.86 | 0.27 |

Table 3. The correlation of $\log_{10} L_{850}$ with $\log_{10} L_{151}$, $\log_{10} L_{[\text{OIII}]}$ and α using Cox’s Proportional Hazard model, the generalized Kendall’s rank correlation test (BHK test) and Buckley–James method for regression with the ASURV program (Isobe, Feigelson & Nelson 1986). χ^2 is the global χ^2 , and P_c is the probability that a correlation is not present for Cox’s Proportional Hazard model. τ is Kendall’s τ , Z is the Z-value and P_k is the probability that a correlation is not present for the BHK test. SD is the standard deviation of the gradient and SDR is the standard deviation of regression for the Buckley–James method.

4 GENERALIZED LUMINOSITY FUNCTIONS

4.1 Definition

The logical extension to the GLF $\rho_Q(L_{151}, L_{[\text{OIII}]}, z) = \rho_Q(\alpha, \beta, z)|J|$, where J is the appropriate Jacobian defined by GRW, is to incorporate submillimetre data and define a GLF ϕ which predicts the number of radio quasars per unit comoving volume (in units of Mpc^3) per unit base-ten logarithm of L_{151} , $L_{[\text{OIII}]}$ and L_{850} at a given redshift z . The PCA (Sec. 3.1) and survival analyses (Sec. 3.2) have demonstrated that the L_{850} – α correlation can be encoded as a linear relation $\log_{10} L_{850}(\alpha) = G\alpha + C$, where G is the gradient and C is the intercept, plus scatter about this relation. We encode the scatter using a Gaussian distribution function about $L_{850}(\alpha)$, with a free parameter σ_L , so that

$$\begin{aligned} \phi(L_{151}, L_{[\text{OIII}]}, L_{850}, z) &= \frac{d^4 N}{d \log_{10} L_{151} d \log_{10} L_{[\text{OIII}]} d \log_{10} L_{850} dV} \\ &= \rho(L_{151}, L_{[\text{OIII}]}, z) f(L_{850}, \alpha, \sigma_L), \end{aligned} \quad (1)$$

where

$$\begin{aligned} f(L_{850}, \alpha, \sigma_L) &= \frac{1}{\sigma_L \sqrt{2\pi}} \exp\left(-\frac{[\log_{10} L_{850} - \log_{10} L_{850}(\alpha)]^2}{2\sigma_L^2}\right), \end{aligned} \quad (2)$$

and dV represents the comoving volume element at an epoch corresponding to redshift z .

Given the large proportion of data with only upper limits at $850 \mu\text{m}$, we need to adapt this GLF so that it takes non-detections properly into account. We will assume that an observer will measure a flux density S_{obs} at $850 \mu\text{m}$ (after correction for synchrotron contamination) which is drawn from a Gaussian distribution about the actual flux density S_{850} with the standard deviation given by the observational error σ_{obs} . Thus, an observed value of flux density S_{obs} could be due to a range of real (synchrotron-corrected) flux density S_{850} , each of which corresponds to a luminosity L_{850} (assuming β_d and T_d from Priddey & McMahon 2001). In this way, we define a new GLF Φ in terms of S_{obs} and observational error σ_{obs} , related to the GLF ϕ by

$$\begin{aligned} \Phi(L_{151}, L_{[\text{OIII}]}, S_{\text{obs}}, \sigma_{\text{obs}}, z) &= \int \phi(L_{151}, L_{[\text{OIII}]}, L_{850}, z) g(S_{\text{obs}}, S_{850}, \sigma_{\text{obs}}) |J'| dS_{850}, \end{aligned} \quad (3)$$

where

$$\begin{aligned} g(S_{\text{obs}}, S_{850}, \sigma_{\text{obs}}) &= \text{Prob}(S_{\text{obs}} | S_{850}, \sigma_{\text{obs}}) \\ &= \frac{1}{\sigma_{\text{obs}} \sqrt{2\pi}} \exp\left(-\frac{[S_{\text{obs}} - S_{850}]^2}{2\sigma_{\text{obs}}^2}\right), \end{aligned} \quad (4)$$

and $|J'|$ is the new Jacobian needed to convert from S_{850} to $\log_{10} L_{850}$.

4.2 Normalization corrections

One of the known small problems with the GLFs defined by GRW is that they predict too few objects at low redshift, and correspondingly too many objects at high redshifts in comparison to the 3CRR, 6CE and 7CRS data. This was a consequence of trying to fit the 6C and 7C source counts (in addition to the 3CRR, 6CE and 7CRS redshift surveys) and may reflect imperfections in the evolutionary model used for the high- α population (GRW). Since the redshift range of our sample is $1.37 < z < 3.5$, and we have only a small sample of objects, we expect that such imperfections may be important. Table 4 shows how we have attempted to correct for this effect by scaling the sky areas of each subsample by the ratio of the total number of objects in each subsample to the nearest whole number of objects (quasars and radio galaxies) predicted by the unified schemes for each of the models (2RS, 2SS and 2RR; see Table 4 of GRW). Note that we do not yet know the number of radio galaxies in the TOOT surveys in this redshift range, so we have estimated the correction factor by using the average quasar fraction, from the three models, to predict the number of TOOT radio galaxies from the number of TOOT quasars.

4.3 Results

The GLF of Eqn. 1 was combined with each of the three models (2RS, 2SS and 2RR) defined in Table 4 of GRW using the best-fitting unified scheme parameters found in their Table 5. A maximum-likelihood analysis was performed in order to find best-fitting values of σ_L , G and C . The likelihood function η was defined as

$$\begin{aligned} \eta = & -2 \sum_{i=0}^{18} \ln[\Phi(L_{151i}, L_{[\text{OIII}]i}, S_{\text{obs}i}, \sigma_{\text{obs}i}, z_i)] \\ & + 2 \iiint \int [\phi(L_{151}, L_{[\text{OIII}]}, L_{850}, z) \Omega(L_{151}, z) \\ & \times \frac{dV}{dz} dz d(\log_{10} L_{151}) d(\log_{10} L_{[\text{OIII}]}) d(\log_{10} L_{850})] \end{aligned} \quad (5)$$

where Ω is the sky area available for each sample of radio sources, modified by the factors derived from Table 4.

The best-fitting values of the three free parameters σ_L , G and C were found to be almost identical for each of the three models and are presented in Table 5. The steeper gradient and different normalization of this line compared to that found by the survival analysis can be explained by our new method of treating upper limits which means that non-detections can be drawn from a wide range of underlying submillimetre luminosities.

A probability distribution was found for the gradient G of the L_{850} versus α correlation by marginalising the likelihood (the function η in Eqn. 5) over C and σ_L , and normalizing. Fig. 3 shows that the probability that there is a positive correlation ($S > 0$) between L_{850} and α is ~ 99 per cent. Note that this is a different conclusion than one would draw from the ‘formal’ error from Table 5 because marginalization allows correctly for the complicated shape of the probability distributions. Note, however, that there is still quite a large error on the gradient G of the correlation.

The relative probability of the models with a receding

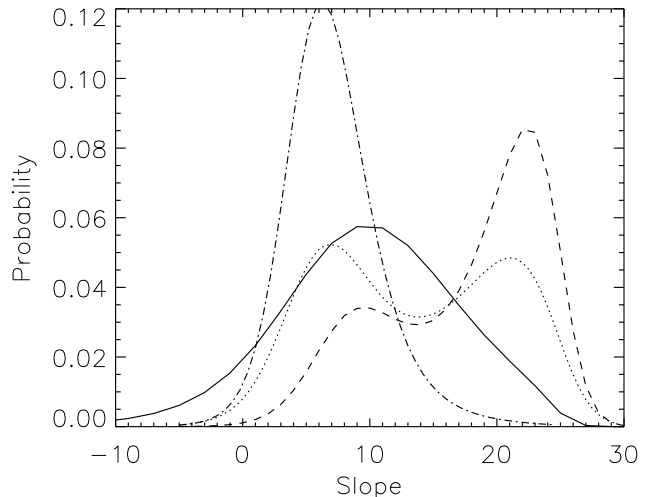


Figure 3. Marginalized probability distributions for the gradient G of the $\log_{10} L_{850} - \alpha$ correlation derived from the 2RS GLF (similar probability distributions can be inferred using models 2RR and 2SS). Different datasets have been used: the radio quasars from Table 1 (dot-dashed line); dataset A (dotted line); B (solid line); and C (dashed line). Datasets A, B and C are defined in Sec. 5.1.

torus in the high- α population (models 2RS and 2RR) with respect to the GLF with a non-luminosity-dependent unified scheme in both populations (model 2SS) is ~ 100 . The main reason for this is that the adoption of a receding torus means that the value of the transition angle Θ_{trans} increases with α , and as all the radio quasars in the sample have high values of α (Fig. 2), Eqn. 10 of GRW implies a corresponding boost in the values of ρ_Q [note that the free parameter fixing the behaviour of Θ_{trans} has not been allowed to vary in our new likelihood analysis]. However, in complete samples, these increased likelihoods of seeing radio quasars goes hand-in-hand with decreased likelihoods of seeing radio galaxies (see Fig. 8 of GRW), so we defer interpretation of any difference in likelihoods until, in Sec. 5.1, we consider complete samples including both radio quasars and radio galaxies.

5 COMPARISON WITH PREVIOUS STUDIES

5.1 Comparison with the Willott *et al.* sample

Willott *et al.* (2002a) found that radio quasars were a factor of ~ 5 times brighter than radio galaxies in the submillimetre, based on SCUBA observations of eleven 3CRR, 3CR and 6CE quasars (see the lowest rows of Table 1) and twelve 3CRR and 6CE radio galaxies (Table 6). This factor could be reduced somewhat by adopting larger estimates of synchrotron contamination, but not below a factor ~ 2 , and so not to the point where radio quasars and radio galaxies have comparable dust luminosities. We next make a comparison of the ability of the three GLFs to reproduce the distribution of submillimetre fluxes of these data. A one-dimensional optimization algorithm (the Golden Section Search method; Press *et al.* 1992) was used to find the best-fitting value of σ_L , using the data (on both radio quasars and radio galaxies) presented by Willott *et al.* (2002a). As these radio quasars

| | 3CRR | | 6CE | | 7CRS | | TOOT | | Total | |
|------|-------|-------|------|------|------|------|-------|-------|-------|-------|
| | Q | RG | Q | RG | Q | RG | Q | RG | Q | RG |
| Data | 9 | 7 | 2 | 5 | 2 | 0 | 5 | ? | 18 | ? |
| 2RS | 12.38 | 8.23 | 7.13 | 5.18 | 2.64 | 1.92 | 7.88 | 21.24 | 32.05 | 38.04 |
| 2SS | 8.24 | 12.23 | 7.71 | 5.39 | 2.58 | 1.87 | 11.37 | 17.75 | 31.06 | 39.27 |
| 2RR | 12.65 | 7.97 | 7.41 | 5.37 | 2.58 | 1.88 | 8.26 | 20.86 | 33.12 | 37.19 |
| 2RS | 9.43 | 6.27 | 4.53 | 2.31 | 0.78 | 1.28 | 4.35 | 11.72 | 19.07 | 21.99 |
| 2SS | 6.28 | 9.32 | 4.72 | 2.26 | 0.81 | 1.25 | 6.27 | 9.79 | 18.37 | 22.85 |
| 2RR | 9.64 | 6.07 | 4.70 | 2.26 | 0.81 | 1.25 | 4.56 | 11.51 | 19.70 | 21.49 |

Table 4. Table of the number of radio quasars (Q) and radio galaxies (RG) from each survey in the sample (upper panel) and the predicted numbers of quasars and radio galaxies in each subsample before and after (middle and lower panels respectively) a factor was applied to the sky areas to correct for the imperfections in the GLFs at high redshifts (Sec. 4.2); see GRW for a full description of the three models (2RS, 2SS, 2RR) which represent the three different unified schemes. Note that the number of radio galaxies in the relevant redshift range is not yet established for the TOOT survey.

| Model | σ_L | G | C | η_{\min} | $\det(\nabla\nabla\eta_{\min})$ | P_{2RS} |
|-------|---------------------------|-------------------|--------------------|---------------|---------------------------------|-----------|
| 2RS | $0.365^{+0.138}_{-0.101}$ | 6.036 ± 5.180 | 22.136 ± 0.493 | 651.79 | 1534.28 | 1.000 |
| 2SS | $0.365^{+0.138}_{-0.101}$ | 6.036 ± 5.180 | 22.136 ± 0.493 | 661.37 | 1534.27 | 0.009 |
| 2RR | $0.365^{+0.138}_{-0.101}$ | 6.036 ± 5.180 | 22.136 ± 0.493 | 652.04 | 1534.28 | 0.886 |

Table 5. Results of the likelihood analysis of Sec. 4.3 which is based on the sample of radio quasars in Table 1. The best-fitting values of the parameters σ_L , G and C , the minimum value of the likelihood function η_{\min} corresponding to these best-fitting values and $\det(\nabla\nabla\eta_{\min})$ for the three unified schemes. ‘Formal’ error bars on the parameters are obtained from the $\nabla\nabla\eta$ matrix in the normal manner (see GRW), and the probability P_{2RS} of each of the models with respect to model 2RS is calculated using Equation 12 of GRW.

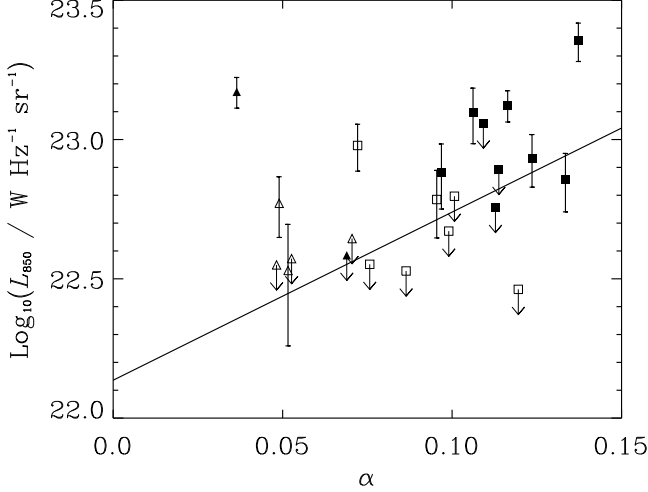


Figure 4. The 850 μ m luminosity L_{850} against α for the sample of eleven quasars (last 11 rows of Table 1) and twelve radio galaxies (Table 6) considered by Willott et al. (2002a) with symbols as in Fig. 1. 2σ upper limits are shown for the non-detections. The best-fitting line from the optimization procedure is shown (solid line; see Sec.5.1).

and radio galaxies now span a much smaller range in α , compared to the full sample used to constrain the gradient G and offset C (Sec. 4.3), we initially kept the best-fitting values of G and C constant during this optimization.

We present the results in Table 7. Fig. 4 shows this sample with the best-fitting gradient determined by the optimization procedure in Sec. 4.3. Note that the addition of the radio galaxies leads to a small increase in the derived scatter σ_L in the relationship between L_{850} and α , but that the scatter is still insufficient to hide what appears to be

| Model | σ_L | η_{\min} | $\det(\nabla\nabla\eta_{\min})$ | P_{2RS} |
|-------|---------------------------|---------------|---------------------------------|-----------|
| 2RS | $0.481^{+0.197}_{-0.140}$ | 876.88 | 45.2 | 1.000 |
| 2SS | $0.481^{+0.197}_{-0.140}$ | 884.57 | 45.2 | 0.028 |
| 2RR | $0.481^{+0.197}_{-0.140}$ | 877.45 | 45.2 | 0.752 |

Table 7. Results of the likelihood analysis of Sec. 5.1 which is based on the radio quasars and radio galaxies in the sample of Willott et al. (2002a). The best-fitting parameter σ_L , the minimum value of the likelihood function η_{\min} corresponding to this value and $\det(\nabla\nabla\eta_{\min})$ for the three unified schemes. ‘Formal’ error bars on the parameters are obtained from the $\nabla\nabla\eta$ matrix in the normal manner (see GRW), and the probability P_{2RS} of each of the models with respect to model 2RS is calculated using Equation 12 of GRW.

a significant difference in the L_{850} values of radio quasars and radio galaxies. For this sample, we find that models with a receding torus in the high- α population (2RS and 2RR) are strongly favoured (by a factor of ~ 40) over a model with a torus which has a constant opening angle in the high- α population. This constrasts with the very marginal (factor ~ 2) difference in likelihoods between such models in GRW. Since, essentially, the L_{151} and $L_{\text{[OIII]}}$ data considered are a subset of the data considered by GRW, and (in contrast to the likelihood analysis of Sec. 4.3) both radio quasars and radio galaxies are included, the reason that we are reaching such a different conclusion is that this current study focuses on luminosity differences between radio quasars and radio galaxies in just the high- α population. The use of a relatively narrow range of redshifts, so that the confusions associated with mixing low- and high- α populations and with wide ranges of redshift is an additional factor, as is the additional constraint of the submillimetre properties. Willott et al. (2002a) attributed the difference in submillimetre flux-densities between radio quasars and radio

| Name | Class | Redshift z | D / kpc | $\log_{10}[L_{151}/$ $\text{WHz}^{-1}\text{sr}^{-1}]$ | $\log_{10}[L_{\text{[OIII]}}/$ $\text{W}]$ | $S_{850}/$ mJy | $S_{450}/$ mJy | SC | α | β |
|--------------|-------|-----------------|--------------|--|---|------------------------|--------------------|------|----------|---------|
| 4C 13.66 | G | 1.450 | 50.7 | 28.09 | 36.63 | 3.53 \pm 0.96 | -16.20 ± 18.20 | 0.00 | 0.095 | 0.010 |
| 3C 329 | G | 1.781 | 94.6 | 28.42 | 36.38 | 0.83 \pm 1.00 | -2.10 ± 18.30 | 0.00 | 0.099 | 0.031 |
| 3C 241 | G | 1.617 | 7.7 | 28.11 | 36.75 | 1.81 \pm 0.94 | 14.80 ± 12.60 | 0.00 | 0.101 | 0.006 |
| 3C 294 | G | 1.786 | 126.7 | 28.39 | 36.97 | 0.19 \pm 0.78 | 5.40 ± 13.40 | 0.00 | 0.120 | 0.008 |
| 3C 322 | G | 1.681 | 279.4 | 28.21 | 35.97 | -0.05 ± 1.06 | -37.50 ± 16.00 | 0.00 | 0.076 | 0.038 |
| 3C 437 | G | 1.480 | 291.0 | 28.11 | 36.37 | -1.18 ± 0.98 | 2.90 ± 17.30 | 0.00 | 0.086 | 0.020 |
| 3C 470 | G | 1.653 | 203.2 | 28.15 | 35.93 | 5.64 \pm 1.08 | 57.80 ± 32.90 | 0.00 | 0.072 | 0.037 |
| 6C 0820+3642 | G | 1.860 | 193.8 | 27.55 | 36.01 | 2.07 \pm 0.96 | 13.60 ± 18.00 | 0.00 | 0.052 | 0.011 |
| 6C 0901+3551 | G | 1.904 | 21.9 | 27.46 | 36.13 | -1.83 ± 1.15 | -19.30 ± 8.20 | 0.00 | 0.053 | 0.003 |
| 6C 0905+3955 | G | 1.882 | 934.5 | 27.71 | 35.77 | 3.62 \pm 0.89 | 31.20 ± 16.20 | 0.00 | 0.049 | 0.026 |
| 6C 0919+3806 | G | 1.650 | 88.1 | 27.53 | 35.93 | -0.88 ± 1.05 | 10.50 ± 10.10 | 0.00 | 0.048 | 0.014 |
| 6C 1204+3708 | G | 1.779 | 435.2 | 27.61 | 36.45 | 0.16 \pm 1.25 | 45.10 ± 26.60 | 0.00 | 0.070 | -0.003 |

Table 6. Submillimetre observations and basic data for the sample of twelve radio galaxies from Willott et al. (2002a). The values for the [OIII] line strength have been calculated by various methods (see Sec. 2). Submillimetre detections at the $\geq 2\sigma$ level are given in bold type. SC is the assumed fractional synchrotron contamination at 850 μm . D is the projected linear size and a \dagger denotes that it is measured between the core and an extended component on just one side of the core. contaminations, expressed as fractions of observed S_{850} , were taken from Rawlings et al. (2004); α and β are the parameters defined by GRW.

galaxies to the dust being heated by quasars (rather than by starbursts) which would cause emission-line luminosities to be correlated with submillimetre luminosities if both reflect the luminosity of the central source. This result is consistent with a receding torus because objects with more luminous emission lines are more likely to be viewed as quasars, because of the larger torus opening angles, and therefore to have higher $L_{\text{[OIII]}}$, α and L_{850} .

The weighted mean of the synchrotron-corrected submillimetre fluxes for the radio quasars in the Willott et al. (2002a) sample is 4.72 ± 0.36 mJy, and for the radio galaxies it is 1.25 ± 0.29 mJy; the median is 4.47 mJy for quasars and 0.51 mJy for radio galaxies. We have simulated distributions of S_{850} from the average of 30 simulations using each of the three GLFs. For model 2SS, the shift is ≈ 0 mJy with the median S_{850} being 3 mJy for both radio quasars and radio galaxies. This is as expected because, without a receding torus, experiments that focus only on the high- α population would find no difference in the α and hence S_{850} values of radio quasars and radio galaxies. We find that the shift in S_{850} between the median quasar and the median radio galaxy is 1.0 mJy for models 2RR and 2RS (the median quasar has a flux density of 3.0 mJy and the median radio galaxy has a flux density of 2.0 mJy), so that quasars are predicted to be 1.5-times brighter in the submillimetre than radio galaxies. Encouragingly, then, shifts in the direction seen in the data are predicted, but not by a large enough factor. It is easy to see how this factor has arisen. The median α is 0.113 for quasars and 0.074 for radio galaxies due a larger median emission line luminosity of $\log_{10}(L_{\text{[OIII]}}/\text{W}) = 37.00$ for quasars than the corresponding value of 36.25 for radio galaxies, with relatively well-matched radio luminosities [median $\log_{10}(L_{151}/(\text{WHz}^{-1}\text{sr}^{-1}))$ for quasars of 28.19 compared to 28.10 for radio galaxies]. Using the best-fitting $L_{850} - \alpha$ relation, this difference in α leads to median $\log_{10}(L_{850}/\text{WHz}^{-1}\text{sr}^{-1})$ of 22.82 for quasars and 22.58 for radio galaxies - a difference of 0.24 or a factor of ≈ 1.7 .

It follows that the optimized gradient for the strength of the $L_{850} - \alpha$ correlation may not be high enough to reproduce the submillimetre difference seen by Willott et al. (2002a). However, this gradient was derived based on quasar data

alone, and we have seen from the error bars given in Table 5, and the width of the marginalized probability distribution in Fig. 3, that there is a large uncertainty in these values. We therefore repeated the optimization procedure with three free parameters (σ_L , G and C) and for three datasets defined as follows: (A) the eighteen quasars from Table 1 and the twelve radio galaxies from Table 6; (B) the eleven quasars and the twelve radio galaxies from Willott et al. (2002a); and (C) the same dataset as (A), but excluding one radio quasar, 6C 1045+3513, the most prominent outlier in Fig. 5.

In Table 8 we present the results of the optimization procedure, and the lines using these best-fitting gradients and offsets are plotted in Fig. 5. We find that models 2RS, 2RR and 2SS all give very similar optimized parameters for a given dataset (A, B or C), and that for all datasets models with a receding torus (either 2RR or 2RS) in the high- α population are favoured strongly over the 2SS model. Formal errors could not be found for the gradient G and the offset C for dataset B because the range in α for this dataset is so small that the likelihood surfaces are not well described by a multi-dimensional-Gaussian approximation. To find an error on G (given in the brackets in Table 8), we fitted a Gaussian to the marginalized probability distribution of the gradient (Fig. 3); the probability distributions for G given the 2RR model and the various datasets are very similar. The error on C , given in the brackets in Table 8, is a rough estimate based on the expectation that it is greater than that for dataset A, because of the small range in α , but not as great as that for dataset C, which arises because of the double-peaked shape of the probability distribution which is more pronounced than that for dataset A (Fig. 3). These peculiar double-peaked shapes arise because of the large fraction of upper limits in the datasets. Note, however, that for all datasets, a gradient of zero is strongly disfavoured because the upper limits are concentrated at low values of α . Note also, that the secondary peaks at $S \sim 20$ are strongly disfavoured by the statistical detection of the TOOT quasars in the submillimetre by Rawlings et al. (2004), so ignoring these, the peaks in the marginalized probability distributions all cluster in the range $6 \lesssim G \lesssim 10$.

We see in Fig. 3 that the large uncertainty in the gra-

| Dataset | σ_L | G | C | 2SS: P_{2RS} | 2RR: P_{2RS} |
|---------|---------------------------|------------------|-------------------|----------------|----------------|
| A | $0.475^{+0.149}_{-0.114}$ | 6.64 ± 7.90 | 21.89 ± 0.72 | 0.018 | 0.989 |
| B | $0.393^{+0.169}_{-0.118}$ | $9.91 \pm (7.0)$ | $21.56 \pm (1.0)$ | 0.034 | 0.898 |
| C | $0.438^{+0.145}_{-0.109}$ | 9.41 ± 14.66 | 21.61 ± 1.39 | 0.015 | 1.022 |

Table 8. The best-fitting parameters σ_L , G and C for datasets A, B and C (see Sec. 5.1 for a definition of these datasets). ‘Formal’ error bars on the parameters are obtained from the $\nabla\nabla\eta$ matrix in the normal manner (see GRW), and the probability P_{2RS} of each of the models with respect to model 2RS is calculated using Equation 12 of GRW. Brackets indicate that the error is an estimate, because formal errors could not be found for these parameters (see Sec. 5.1 for a discussion of how these were estimated).

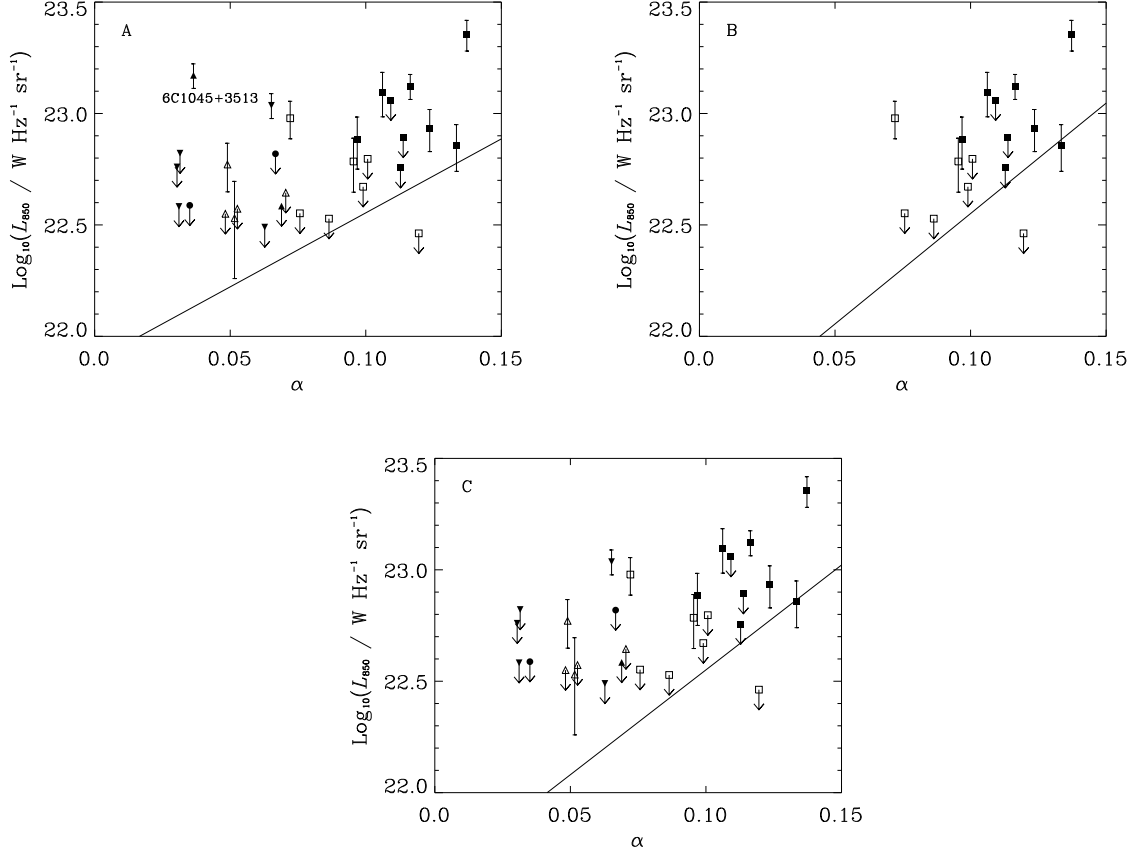


Figure 5. Graphical representation of the results of the optimization procedure described in Sec. 5.1 and Table 8. The lines showing the best-fitting values for the $L_{850} - \alpha$ correlation for datasets A, B and C, are shown alongside the relevant data (symbols as in Fig. 1).

dient G is also compounded by the dramatic influence of just one outlying point (6C 1045+3513). It is interesting that the peak of the probability distribution for G shifts to significantly higher values for datasets B and C, in which this prominent outlier is excluded. It is probable that the submillimetre emission for this object is not dominated by quasar-heated dust (Willott et al. 2002a), but dominated instead by starburst-heated dust. The small size of its radio jets indicate that it is a young radio source in which intense star-formation activity may be synchronized with the jet-triggering event. This hints that the correlation may be strongest for more typical radio sources in which quasar-heated dust may dominate even at the longer wavelengths probed in the submillimetre.

Simulations of the $S_{850} - L_{151}$ plane using the optimized parameters from dataset C were performed. Once more, as expected, the 2SS scheme gives identical values

of S_{850} (≈ 3.40 Jy) for radio quasars and radio galaxies. For the other schemes, larger shifts are confirmed: an average observed flux S_{850} of 4.65 Jy for radio quasars and only 2.09 Jy for radio galaxies for 2RS; and 4.39 Jy for radio quasars and 2.20 Jy for radio galaxies for 2RR. Moreover, Fig. 3 shows that it is perfectly plausible that the true gradient is large enough that the difference in submillimetre luminosities of radio quasars and radio galaxies could easily be by a factor $\gtrsim 2$. Accounting for residual uncertainties in the corrections for synchrotron contamination (Willott et al. 2002a), the factor $\sim 2 - 5$ difference in submillimetre luminosities seen by Willott et al. (2002a) are now in quantitative accord with both the 2RS and 2RR models.

5.2 Comparison with ‘matched-pair’ experiments

We consider in this section whether the GLFs described in Sec. 4 can reproduce the results of Meisenheimer et al. (2001) and van Bemmél, Barthel & de Graauw (2000).

Meisenheimer et al. (2001) observed ten pairs of 3CR radio galaxies and radio quasars with ISOPHOT on ISO at infrared wavelengths between 5 and 180 μm . The sources were matched in redshift and 178-MHz luminosity L_{178} , but spanned a large redshift range of $0.05 < z < 2.02$. The average value of 100-micron flux density S_{100} was 293 mJy for quasars and 300 mJy for radio galaxies, leading to their conclusion that quasars and radio galaxies cannot be distinguished by their observed mid- and far-infrared properties. However, if we use $\beta_d \approx 2$ and the values of dust temperatures found by fitting to the data in Meisenheimer et al. (2001) [if no values were given, a value of 40 K was assumed], we find that the average (rest-frame) 100- μm luminosity L_{100} was 38.69 for quasars and 38.36 for radio galaxies, so that their radio quasars are an average of ~ 2 -times more luminous than radio galaxies at 100 μm .

We simulated histograms of $\log_{10} L_{100}$ for the Meisenheimer et al. (2001) dataset from the average of 30 simulations using the optimized parameters for dataset C (Sec. 5.1). For 2SS, it is 38.57 for radio quasars and 38.39 for radio galaxies, with a shift of 0.18 because the range of z is sufficiently large that the low- and high- α populations become mixed, as was the case for the experiments of GRW. For 2RS, the median L_{100} is 38.75 for quasars and 38.27 for radio galaxies giving a shift of 0.48. For 2RR, it is 38.75 for quasars and 38.21 for radio galaxies, with a shift of 0.54, so that for all models, radio quasars are expected to be brighter than radio galaxies, in agreement with the data. To try and account for the effects of the selection of matched pairs, we used the GLFs to pick a value of L_{100} (by extrapolating from the value of L_{850} using our canonical dust spectrum) from the actual redshift and L_{178} values of each quasar and radio galaxy in the Meisenheimer et al. (2001) sample. We find that in only ≈ 60 per cent of the pairs, is the quasar brighter than the radio galaxy in L_{100} , based on one thousand simulations of picking the 10 pairs. This shows that the matched pairs method is not very effective at discovering quite large differences in the properties of radio quasars and radio galaxies.¹

A similar ‘matched pair’ experiment was performed at lower redshift ($0.25 < z < 0.55$) by van Bemmél, Barthel & de Graauw (2000). They obtained ISOPHOT data for four pairs of 3CR radio galaxies and radio quasars, matched in 178 MHz luminosity and redshift. They concluded that broad-lined objects were brighter in the far-infrared than narrow-lined objects, since the average 90- μm luminosity L_{90} was 37.90 for radio quasars and ≤ 37.76 for radio galaxies. Simulating their experiment using our GLFs we could reproduce this measured difference between radio quasars and radio galaxies for any of the unified schemes. We note that the sample of van Bemmél, Barthel & de Graauw (2000) contains such a

small number of objects that it would be very difficult to reach significant conclusions from such an experiment.

In conclusion, existing matched-pair experiments typically mix low- and high- α populations so all the GLFs predict a luminosity difference between radio quasars and radio galaxies at 100 μm . We have seen that using small numbers of matched pairs is not a particularly good way of comparing unified schemes, but that the results from such methods are consistent with the other results described in this paper.

6 SCALING RELATION BETWEEN L_{850} AND L_{BOL}

Here, we derive a rough scaling relation between L_{850} and bolometric quasar luminosity L_{BOL} for the high- α radio source population, argue that it may be applicable to quasars in general, and suggest how it might physically arise.

The form of the underlying L_{850} – L_{BOL} relation can be inferred from the gradient G (Table 8; Fig. 3). Using the value of G derived from dataset C (see Sec. 5.1), we find that

$$\alpha \propto \frac{1}{9.41} \log_{10} L_{850}. \quad (6)$$

From Equations 1 and 2 of GRW, we have another expression for α

$$\alpha \propto \frac{1}{s_1 \sqrt{2\sqrt{n}}} \log_{10} L_{151} + \frac{1}{s_2 \sqrt{2\sqrt{n}}} \log_{10} L_{[\text{OIII}]}, \quad (7)$$

in which $s_1 = 1.05$, $s_2 = 1.10$, and $n = 302$.

From Equation 4 of GRW, we find that

$$\log_{10} L_{[\text{OIII}]} \propto 1.045 \log_{10} L_{151}, \quad (8)$$

so that if we assume that $L_{\text{BOL}} \propto L_{[\text{OIII}]}$, then

$$L_{850} \propto L_{\text{BOL}}^{0.7 \pm 0.2}, \quad (9)$$

where the 1σ -error bar has been estimated from the probability distribution of the gradient (Fig. 3, ignoring the secondary peak) rather than from the value from the covariance matrix. Note that adoption of dataset A would be consistent with Eqn. 9, but would favour gradients towards the lower end of the quoted error bar. Note also that values derived from secondary peaks in the marginalized probability distributions of G are inconsistent with the constraints set from considering the sample consisting of only radio quasars [see Fig. 3 and the statistical detection of TOOT quasars by Rawlings et al. (2004)], and seem likely to be artefacts of the small ranges in α probed by submillimetre-detected objects in the relevant datasets. The scaling relation of Equation 9 is in good agreement with the results of Sec. 3.1 in which it was found that the first principal component represented a linear (roughly equal weight) combination of normalized versions of $\log_{10} L_{151}$, $\log_{10} L_{[\text{OIII}]}$ and $\log_{10} L_{850}$, meaning that the three variables scale-up with each other according to power laws with indices given roughly by the ratios of the associated data standard deviations, namely $\sim 1 : 1 : 0.6$ (assuming the real values of $\log_{10} L_{850}$ lie close to their $1-\sigma$ upper limits).

The derived L_{850} – L_{BOL} scaling relation is similar to that inferred from the correlation between L_{850} and the optical luminosity of radio-quiet quasars:

¹ Note also that in one of the Meisenheimer et al. (2001) matched pairs, 3C 325 (the brighter far-IR source of its pair) is taken to be a radio galaxy, whereas our new optical spectroscopic data (Appendix A) suggests it is a reddened quasar.

Willott, Rawlings & Grimes (2003) found a factor ~ 1.4 reduction in L_{850} per unit drop in absolute blue magnitude M_B , which corresponds to $L_{850} \propto L_{\text{Bol}}^{0.4}$ if we assume that L_{Bol} scales linearly with the observed optical luminosity. This suggests that the scaling relation derived here is not peculiar to radio-selected objects, but is a generic feature of AGN.

There is one obvious way in which this scaling might arise. Consider models in which the observed submillimetre luminosity of powerful AGN comes from the dust in the obscuring torus as a result of direct quasar heating. As suggested previously by Simpson & Rawlings (2000), a receding-torus-like scheme means that the solid angle subtended by the torus scale with radius r and hence L_{Bol} as $h/r \propto L_{\text{Bol}}^{-0.5}$ for constant torus half-height h . If the fraction of the radiation re-processed by the dust torus is simply proportional to this solid angle, then the implied scaling relation is $L_{850} \propto L_{\text{Bol}}^{0.5}$. This is within the errors of the value observed (Eqn. 9). Of course, more realistic receding torus models might feature distributions in h and/or systematic variations of h with L_{Bol} (Simpson 2003), and hence predict slightly different scaling relations

7 CONCLUSIONS

In this paper, the generalized-luminosity-function (GLF) approach of GRW has been extended to predict the number density of low-radio-frequency-selected quasars and galaxies as a function of redshift, radio luminosity, emission-line luminosity and 850- μm luminosity, or observed 850- μm flux density and sensitivity, using a new method which enables us to use data with upper flux-density limits. The new free parameters in these extended GLFs were fixed by comparison with SCUBA (850- μm) data on high-luminosity, high-redshift radio sources. Results from our GLF approach were found to reproduce previous comparative studies of the submillimetre and far-infrared luminosities of radio quasars and radio galaxies (Willott et al. 2002a; Meisenheimer et al. 2001; van Bemmell, Barthel & de Graauw 2000).

We find robust evidence that the submillimetre luminosity of low-frequency-selected radio sources is correlated with the GRW α parameter, and hence the bolometric quasar luminosity L_{Bol} via a scaling relation $L_{850} \propto L_{\text{Bol}}^{0.7 \pm 0.2}$. This corresponds to a factor of $\approx 1.9 \pm 0.3$ reduction in L_{850} per unit drop in absolute blue magnitude M_B which is similar to the correlation tentatively identified for the radio-quiet quasar population (Willott, Rawlings & Grimes 2003). The fact that the gradient of the scaling relation is less steep than a proportionality may give clues as to how L_{850} arises, and is consistent with models in which quasar heating dominates, and in which dust in the receding torus intercepts and re-processes a lower fraction of the bolometric luminosity into the mid- and far-infrared bands.

We also find robust evidence that a receding-torus-like scheme is strongly favoured (by a factor ~ 40 in probability over models without a receding torus) in the high- α population of a two-population scheme for radio sources. In such schemes, radio quasars are brighter in narrow emission lines and submillimetre luminosity (than radio galaxies matched in radio luminosity and redshift) because they are biased to-

wards the objects with the highest values within the spread of bolometric luminosity.

ACKNOWLEDGEMENTS

JAG was supported by a graduate studentship from Oxford University and Magdalen College. SR thanks the PPARC for a Senior Research Fellowship. We thank Matt Jarvis and Chris Simpson for useful conversations, and the anonymous referee for a very useful report. This research has made use of the NASA/IPAC Extragalactic Database, which is operated by the Jet Propulsion Laboratory, Caltech, under contract with the National Aeronautics and Space Administration.

REFERENCES

- Efstathiou A., Rowan-Robinson M., 1994, MNRAS, 266, 212
- Grimes J.A., Rawlings S., Willott C.J., 2004, MNRAS, 349, 503
- Hes R., Bathel P.D., Fosbury R.A.E., 1993, Nat, 362, 326
- Hill G.J., Rawlings S., 2003, New Astronomy Reviews, 47, 373
- Isobe T., Feigelson E.D., Nelson P.I., 1986, ApJ, 306, 490
- Laing R.A., Riley J.M., Longair M.S., 1983, MNRAS, 204, 151
- Lawrence A., 1991, MNRAS, 252, 586
- McCarthy P.J., 1993, ARAA, 31, 639
- Meisenheimer K., Haas M., Müller S.A.H., Chini R., Klaas U., Lemke D., 2001, A&A, 372, 719
- Press W.H., Teukolsky S.A., Vetterling W.T., Flannery B.P., 1992, Numerical Recipes: The Art of Scientific Computing. Cambridge Univ. Press, Cambridge
- Priddey R.S., McMahon R.G., 2001, MNRAS, 324, L17
- Rawlings S., Eales S.A., Lacy M., 2001, MNRAS, 322, 523
- Rawlings S., Hill G.J., Willott C.J., 2004, AJ, to be submitted
- Rawlings S., Willott C.J., Hill G.J., Archibald E.N., Dunlop J.S., Hughes D.H., 2004, MNRAS, 351, 676
- Simpson C., 1998, MNRAS, 297, L39
- Simpson C., 2003, New Astronomy Reviews, 47, 211
- Simpson C., Rawlings S., 2000, MNRAS, 317, 1023
- Spinrad H., Djorgovski S., Marr J., Aguilar L., 1985, PASP, 97, 932
- van Bemmell I., Barthel P., 2001, A&A, 379, L21
- van Bemmell I., Barthel P., de Graauw T., 2000, A&A, 359, 523
- Willott C.J., Rawlings S., Archibald E.N., Dunlop J.S., 2002a, MNRAS, 331, 435
- Willott C.J., Rawlings S., Grimes J.A., 2003, ApJ, 598, 909
- Willott C.J., Rawlings S., Jarvis M.J., 2000, MNRAS, 313, 237
- Willott C.J., Rawlings S., Blundell K.M., Lacy M., 2000, MNRAS, 316, 449
- Willott C.J., Rawlings S., Blundell K.M., Lacy M., Hill G.J., Scott S.E., 2002b, MNRAS, 335, 1120

APPENDIX A: CORRECTED REDSHIFT AND CLASSIFICATION FOR 3C 325

In this Appendix we present a new optical spectrum of 3C 325 which has allowed us to correct both the redshift and classification of this object. We targeted this object because it is highly unusual amongst high-redshift ($z > 0.5$) radio galaxies in the 3CR catalogue as it has been detected (using ISO) as a luminous far-infrared source (Meisenheimer et al. 2001). High- z radio sources detected in the far-infrared by IRAS and ISO are almost exclusively quasars, sometimes because the far-infrared emission is from a beamed non-thermal component (Hes, Barthel & Fosbury 1993), but sometimes because, as detailed in Willott et al. (2002a) and this paper, radio quasars seem to be genuinely brighter (rest-frame) far-infrared sources than radio galaxies when matched in radio luminosity and redshift. Our previous optical spectroscopy of another anomalous far-infrared-loud 3CR ‘galaxy’, 3C 318, found that this object had an incorrect redshift and classification in the literature, and that the object was actually a $z = 1.574$ reddened quasar (Willott, Rawlings & Jarvis 2000). Prior to this work, 3C 325 was classified as an ‘N’ galaxy with a redshift $z = 0.86$ based on the identification of spectral features with moderate, possibly broad, Mg 2799 and weak [OII] 3727 emission (Spinrad et al. 1985).

3C 325 was observed with the dual-beam ISIS spectrograph on the William Herschel Telescope on 22 April 2003; the R300B and R316R gratings were used. Conditions were photometric with good (≈ 0.8 arcsec) seeing and a 1.5-arcsec slit was used. The telescope was pointed at the known optical identification of 3C 325 (RA 15:49:58.22, DEC +62:41:22.4, J2000.0). The total integration time of the observation was 2700s, split into three separate exposures on each arm. In Figure A1 we show the extracted optical spectrum which was spatially unresolved in the two-dimensional spectrum. The object has many strong emission lines (see Table A1) and therefore an unequivocal redshift of $z = 1.135$; the previously reported redshift is incorrect, presumably because the [NeIV] line was confused with Mg II.

Although the cores of most of the emission lines are narrow there is a definite broad ($\sim 3000 \text{ km s}^{-1}$) component underlying the C III] line, and probably a similar component associated with C IV. The Mg II line maybe dominated by a broad feature but it is hard to be certain because there seems to be a lot of absorption to the blue side of the line. The red continuum has a spectral index of ≈ 2.5 , so this object seems to have all the characteristics of a reddened quasar.

3C 325 is a reddened quasar at $z = 1.135$, and not an ‘N’ galaxy at $z = 0.86$ as previously reported (Spinrad et al. 1985). It is interesting that so many of the far-infrared-loud radio sources at high redshift appear to be in the reddened quasar class, as we have discussed in Willott et al. (2002a).

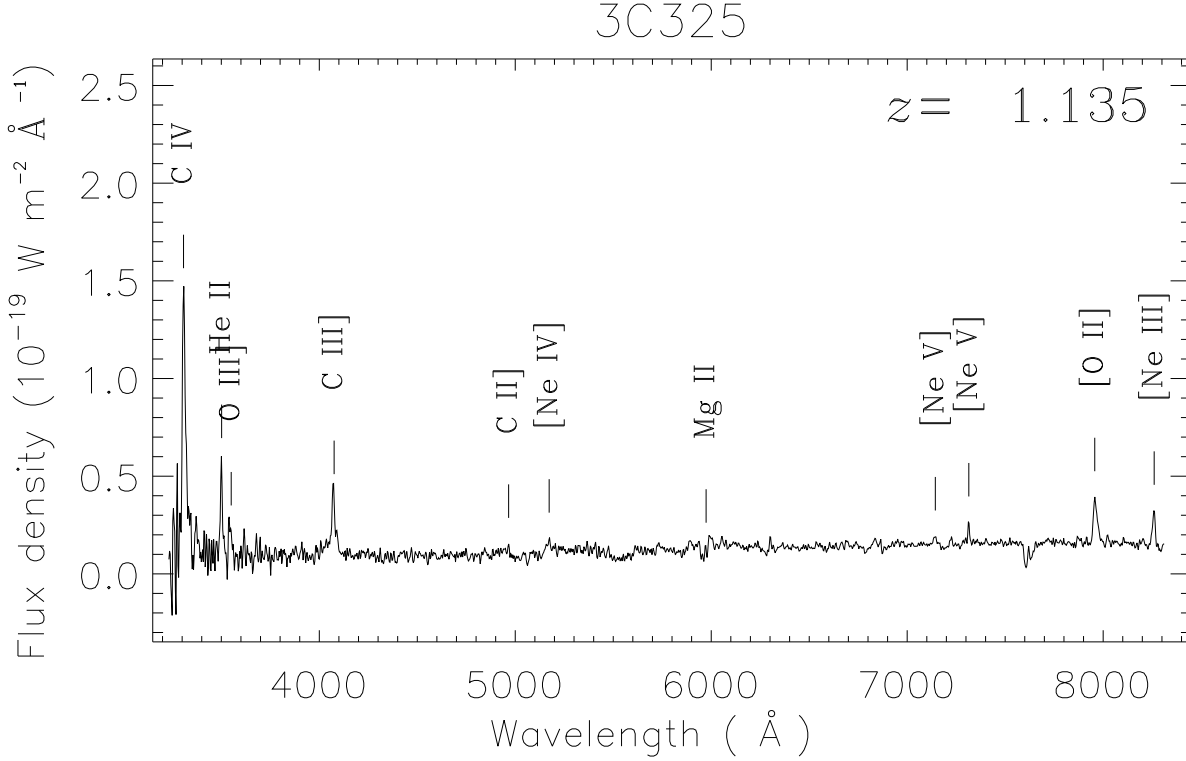


Figure A1. Optical spectrum of the reddened quasar 3C 325, with the emission lines labelled.

| Line | $\lambda_{\text{obs}} / \text{\AA}$ | z_{em} | FWHM / km s^{-1} | Flux $10^{-19} \text{ W m}^{-2}$ |
|---------------|-------------------------------------|-----------------|---------------------------|----------------------------------|
| C IV 1549 | 3309 | 1.136 | 1300† | 42.0 (20) |
| He II 1640 | 3501 | 1.135 | 750 | 8.9 (30) |
| O III] 1663 | 3547 | 1.133 | ? | 2.0 (50) |
| C III] 1909 | 4071 | 1.133 | 800† | 9.0 (30) |
| C II] 2326 | 4966 | 1.135 | ? | 0.8 (60) |
| [Ne IV] 2423 | 5174 | 1.135 | ? | 1.7 (50) |
| Mg II 2799 | 5990 | 1.140‡ | 5000‡ | 4.0‡ (60) |
| [Ne V] 3346 | 7142 | 1.134 | 500 | 0.7 (40) |
| [Ne V] 3426 | 7313 | 1.135 | 400 | 1.2 (30) |
| [O II] 3727 | 7961 | 1.136 | 900 | 8.0 (20) |
| [Ne III] 3869 | 8258 | 1.134 | 600 | 3.8 (25) |

Table A1. Emission line data for 3C 325 from our optical spectrum. Emission line widths have been deconvolved assuming that the source of optical emission was spatially unresolved. † denotes that this refers to the core of a line which appears to have broad wings. ‡ denotes that values are very uncertain because of absorption. The line fluxes have been measured by integrating along the slit direction and no corrections for slit losses have been attempted; estimated errors are expressed, in brackets, as a percentage of the measured flux.